Role of adherend material on the fracture of bi-material composite bonded joints

Lopes Fernandes, Romina; Teixeira de Freitas, Sofia; Budzik, Michal K.; Poulis, Johannes A.; Benedictus, Rinze

Important note
To cite this publication, please use the final published version (if applicable).
Please check the document version above.

Role of adherend material on the fracture of bi-material composite bonded joints

Romina Lopes Fernandes [a], Sofia Teixeira de Freitas [a,*], Michal K. Budzik [b], Johannes A. Poulis [a], Rinze Benedictus [a]

[a] Structural Integrity & Composites Group, Faculty of Aerospace Engineering, Delft University of Technology, P.O. Box 5058, 2600 GB Delft, The Netherlands
[b] Department of Engineering, Aarhus University, Inge Lehmanns Gade 10, 8000 Aarhus C, Denmark

ARTICLE INFO

ABSTRACT

The aim of this study is to investigate the effect of the adherend material on the mode I fracture behaviour of bi-material composite bonded joints. Both single-material (steel-steel and composite-composite) and bi-material (steel-composite) joints bonded with a structural epoxy adhesive are studied. Additionally, two adhesive bondline thicknesses are considered: 0.4 mm (thin bondline) and 10.1 mm (thick bondline). The Penado-Kanninen reduction scheme is applied to evaluate the mode I strain energy release rate. The results show that the mode I fracture energy, G_{Ic}, is independent of the adherend type and joint configuration (single or bi-material). G_{Ic} shows average values between 0.60 and 0.72 N/mm for thin bondlines and 0.90–1.10 N/mm for thick bondlines. For thin bondlines, the failure is cohesive and the similar degree of constraint that is imposed to the adhesive by the high-modulus (i.e., steel) and/or relatively thick (i.e., composite) adherends results in similar values of G_{Ic} for both single- and bi-material joint types. For thick bondlines, the crack grows closer to one of the adhesive-adherend interfaces, but still within the adhesive. The results show that the adhesive could deform similarly, although the crack has been constrained on one side by different types of adherends, either a steel or composite.

1. Introduction

The theoretical understanding and practical robustness of composites have driven research into lightweight construction in the shipbuilding industry. Lighter ships imply, for instance, increased cargo transport and, thus, increased transport efficiency. One possible solution is found to be the replacement of metallic superstructures by composite ones.

Steel used to be the dominating material in the shipbuilding industry. Therefore, the different components used to be welded. The emergence of composites brought initially attention to the mechanical fastening technique and more recently to the adhesive bonding technology. The mechanical fastening technique requires drilling of the composite components, resulting in fibres damage, delamination and non-continuous components, among others. This joining technique also requires fasteners, which leads to a total weight increase. In the adhesive bonding technique, neither fastening holes nor fasteners are needed [1].

The use of adhesive bonding technology in shipbuilding industry results in bonded regions connecting metallic components to composite ones characterized by adhesive layers with a thickness of up to 10 mm. Such adhesive thicknesses are imposed by shipbuilding manufacturing tolerances [2]. For instance, in aerospace and automotive industries, where the manufacturing tolerances are strictly controlled, the bonded regions are much thinner, in general in the sub-millimetre range, than the bonded regions in shipbuilding applications. However, for all applications, the bonded regions are one of the most prone areas for damage initiation. Geometric factors, such as the existence of corners and gradients of materials at the interfaces, lead to stress concentration sites, which may cause cracks to initiate and then propagate within these regions [3]. The peel forces represent the most critical loading case for an adhesive, the mode I loading case, and, hence, are the object of study of this paper.

Structural adhesives, such as epoxies, are being used in shipbuilding applications. These adhesives often exhibit elasto-plastic behaviour. The resistance of the bonded regions against crack initiation and propagation under mode I loading, i.e., the mode I fracture energy, is governed by the stress field ahead of the crack tip. This stress field is affected by the material of the adherends, the adhesive layer thickness, the crack path within the adhesive layer and the crack tip locus direc-

tion. Some extent of the stress field is in the plastic regime and this zone is defined as the plastic process zone. The plastic process zone develops ahead of the crack tip in consequence of adhesive plastifica-tion [4]. The mode I fracture energy, G_{Ic}, is mainly associated with the energy dissipated in forming this zone.

Several studies have focused on the effect of the bondline thickness on the mode I fracture behaviour of bonded joints [5–13]. The effects of the crack path and crack tip locus direction have also been investi-gated by some researchers [14–17]. The subject of the effect of the adherends material on the failure of bonded joints has been mainly investigated for the shear loading case, namely with lap-shear tests [18,19,1,20–25]. These studies addressed the effect of the material of the adherends in two distinct ways: by considering single-material bonded joints with different adherend thicknesses, or by considering bi-material bonded joints. Looking at the effect of the material of the adherends on the mode I fracture behaviour of bonded joints, some studies are available [9,26–31]. However, these studies commonly address the effect of the material of the adherends by considering single-material bonded joints with different adherend thicknesses.

Kawashita et al. [30] investigated the effect of the adherend thick-ness on the mode I fracture energy of metallic joints, bonded with a rubber toughened epoxy adhesive (bondline thickness of 0.25 mm). Three different adherend thicknesses were considered: 0.5, 1, 1.5 mm. It is reported that the lowest value of G_{Ic} corresponds to the lowest adherend thickness, while its value shows independence for thicker adherends. The lowest value of G_{Ic} is justified by the failure type in these specimens. Evidence of interfacial failure was found on the fractured surfaces. Kafkalidis et al. [26] performed fracture exper-iments with steel-steel and aluminium-aluminium double-cantilever beam (DCB) bonded joints. Three different adherend thicknesses were studied. The fracture energy of the bonded joints was found to be inde-pendent of the thickness of the adherends and the adherend material type. The peak stress and the critical displacement for failure sup-ported by the adhesive varied with the constraint level in such a man-ner that the fracture energy remained approximately constant.

Martiny et al. [31] conducted a numerical study on the effects of the adherend stiffness on the fracture behaviour of adhesively-bonded joints, consisting of metallic adherends and an epoxy-based structural adhesive. Two adherend materials were considered: steel and aluminium. In addition, different adherend thicknesses were stud-ied. At a given value of the adhesive layer thickness, the predicted val-ues of G_{Ic} varied by only about 10%, regardless of the adherend material and thickness. The authors explained these results by the higher degree of constraint that is imposed to the adhesive by employ-ing high-modulus and/or relatively thick adherends. Daghyani et al. [9] investigated the constraint effect on the fracture behaviour of a rubber-modified epoxy, via compact tension adhesive joints. The numerically predicted values of G_{Ic} decreased as the adherend stiffness increased. The greater degree of constraint with increasing adherend stiffness led to a lower extent of the plastic-energy dissipation.

Blackman et al. [28] performed mode I fracture tests with single-material DCB bonded joints. Two adherend materials were studied: an unidirectional carbon-fibre reinforced plastic (CFRP) and a mild steel (grade EN24). These adherends were bonded with the same struc-tural epoxy-paste adhesive. The thickness of the bondline was 0.4 mm. All samples failed cohesively, no interfacial failure was observed. The mode I fracture energy appeared to be dependent on the adherend material used. The authors concluded that the different values of the glass transition temperature, T_g, of the cured adhesive in the different bonded joints were the potential cause of the dependence of G_{Ic} with the adherend material. Low volumes of water diffused from the CFRP adherends into the adhesive. The water diffusion interfered with the formation of rubber-particulate separated-phase during the cure of the epoxy adhesive, affecting the T_g and, consequently, the G_{Ic} of the CFRP-CFRP bonded joints [27].

The research carried on up to now addressed the effect of the mate-rial of the adherends on the fracture energy of bonded joints by solely considering single-material bonded joints with different adherend thicknesses. Besides, the studies available are based in standard reduc-tion schemes, such as corrected beam theory or compliance calibration method, which do not take entirely into account the geometric and material properties of the bonded joints, like adhesive bondline thick-ness and out-of-plane stiffness of the adherends. Moreover, to the authors knowledge no studies investigating the possible changes on the fracture energy of bi-material bonded joints are found in open literature.

Therefore, the primary objective of this study is to investigate the effect of the material of the adherends on the mode I fracture beha-viour of adhesively bonded joints by testing single-material (i.e., steel-steel and GFRP-GFRP) and bi-material (i.e., steel-GFRP) joints bonded with a structural epoxy adhesive under DCB fracture test con-ditions. Moreover, two adhesive bondline thicknesses are considered: 0.4 mm (thin bondline) and 10.1 mm (thick bondline). Some speci-mens are instrumented with strain gauges to assess the crack growth process. The Penado-Kanninen (PK) reduction scheme is outlined and applied to evaluate the mode I strain energy release rate, G_I. The morphology of the fractured surfaces is examined by an optical profiler and their chemical composition is analysed by a spectrometer. The results are discussed and conclusions are drawn.

2. Experimental fracture tests

2.1. Specimens

Fig. 1 shows the three DCB configurations tested. The specimens were made of either S690 steel adherends, with a thickness of 3.0 mm, or glass fibre reinforced polymer (GFRP) laminate adherends, with a thickness of 8.6 mm, bonded with a structural two-component epoxy paste adhesive, Araldite 2015 (Huntsman®). Two adhesive bondline thicknesses were studied: 0.4 mm (thin adhesive layer) and 10.1 mm (thick adhesive layer).

The GFRP laminate was manufactured with quadraxial E-glass fab-ric (nominal thickness of 0.9 mm), which consists of a stacking of four unidirectional (UD) layers of E-glass lamina with the orientations $-45°/90°/+45°/0°$, as shown in Fig. 2. A rubber modified epoxy based vinyl ester resin was used to impregnate the E-glass fabric stacking sequence. The GFRP laminate was manufactured by vacuum infusion. After a period of 24 h at laboratory temperature ($\approx 22°C$), the laminate was post-cured at 60 °C during 12 h in an oven, following supplier's recomendations. The mechanical properties of the UD-0° E-glass lam-ina were experimentally determined and are given in Table 1. The mechanical properties of the steel S690 and the epoxy adhesive are listed in Table 2. The steel properties were taken from the supplier's technical datasheet, while the adhesive's mechanical properties were evaluated from tensile dog bone specimens with a thickness of 2 mm in accordance with ISO 527 [32].

The bi-material steel-GFRP DCB configuration was manufactured by following the Strain based design criterion developed by Wang et al. [33] to guarantee pure mode I loading at the crack tip. The Strain based criterion is given by,

$$E_x^{\text{f-adher 1}} h_{\text{adher 1}}^2 = E_x^{\text{f-adher 2}} h_{\text{adher 2}}^2, \tag{1}$$

where $E_x^{\text{f-adher 1,2}}$ is the effective bending modulus of adherend 1 and 2, respectively. In the present study, steel and GFRP adherends are used. Therefore, for the steel adherend, the $E_x^{\text{f-steel}}$ is equal to the material's Young's modulus (see Table 2). The effective bending modulus of the GFRP laminate, $E_x^{\text{f-GFRP}}$, is calculated by applying the classical lamina-tion theory (CLT) [34]. In the case of a non-symmetric lay-up, $E_x^{\text{f-GFRP}}$ is equal to,
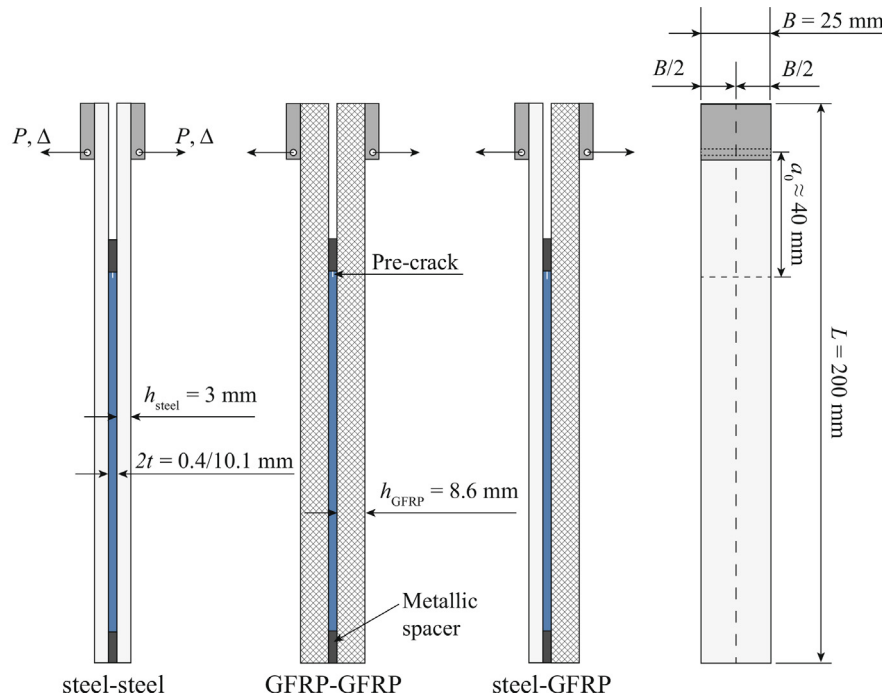
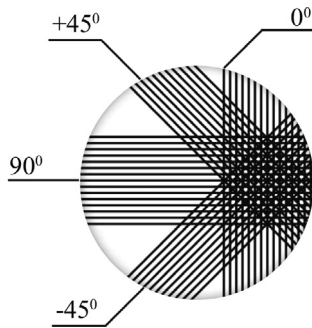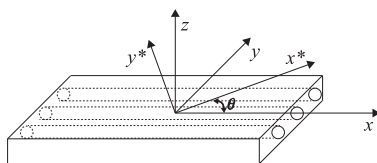**Fig. 1.** DCB specimen: the three tested configurations.

Fig. 2. Quadraxial E-glass fabric representation: stacking of four UD layers of E-glass lamina $-45°/90°/+45°/0°$.

$$E_x^{\mathrm{f-GFRP}} = \frac{12}{h_{\mathrm{GFRP}}^3 J_{44}}, \tag{2}$$

where J_{44} is determined from matrix $[J]$,

$$|J| = \left| \begin{matrix} A & B \\ B & D \end{matrix} \right|^{-1}. \tag{3}$$

The $[A], [B]$, and $[D]$ are called the extensional, coupling and bending matrices, respectively [34].

By taking the steel adherend thickness, h_{steel}, equal to 3 mm, the GFRP adherend is designed to meet the Strain based criterion. The lay-up of the GFRP laminate is given in Table 3 as well as the $E_x^{\mathrm{f-GFRP}}$ and the final thickness of the laminate after post-curing (the final thickness is smaller than the nominal one due to the manufacturing process constraints). For more details about the Strain based criterion and laminate stacking definition, the interested reader is referred to [33].

The surfaces of the steel adherends were grit blasted using aluminium oxide (Corublast Super Z-EW nr. 100). Before and after the

Table 1
Mechanical properties of the UD-0° E-glass lamina.

Material	E_{xx} (MPa)	E_{yy} (MPa)	G_{xy} (MPa)	G_{xz} (MPa)	G_{yz} (MPa)	ν_{xy}
0° E-glass lamina	37861	12047	5003	4125	3692	0.252

Table 2

Mechanical properties of the steel S690 and the epoxy adhesive Araldite 2015.

Material	E (MPa)	ν	$\sigma_{\text{yield}}^{***}$ (MPa)	σ_{ultimate} (MPa)
Steel S690	210000	0.30	770	832
Epoxy adhesive[*]	2000 ± 300	0.33^{**}	16.1 ± 1.9	28.8 ± 0.7

[*] evaluated from dog bone specimens cured 1 h at 80°C
[***] supplier's technical datasheet
[***] Steel: yield strength 0.2%; Adhesive: yield strength 0.1%

Table 3

GFRP laminate: lay-up based on the Strain based design criterion [33] (the lay-up is defined from the bottom to the top of the laminate).

Criterion	Lay-up	h_{GFRP}^{*} (mm)	$E_x^{\text{f-GFRP}}$ (MPa)
Strain based	$[0° +45° \ 90° \ -45°]_5/[+45° \ 90° \ -45° \ 0°]_5$	8.60	21996

h_{GFRP}^{*} – final thickness of the laminate after post-cure cycle.

grit blasting, the surfaces were cleaned with a clean cloth soaked with acetone. Afterwards, the steel surfaces were immersed in a potassium hydroxide solution (alkaline cleaner), which was stirred at 300 rpm and heated to 60 °C. The immersion in the solution lasted 10 min. As a final step prior to bonding, the cleaned steel surfaces were immersed in a silane γ-glycidoxypropyltrimethoxysilane (γ-GPS) solution for 20 s in order to strengthen the adhesion of the adhesive at the interfaces. The steel adherends were then oven cured for 1 h at 150 °C. The silane solution was prepared in three steps according to Li et al. [35]. Firstly, the γ-GPS was hydrolysed in distilled water (DW)-methanol mixture. The volume ratios of γ-GPS/DW/methanol were 10/80/10, respectively. Secondly, the pH was set to 5–5.5 by adding acetic acid to keep the solution's stability. Finally, the solution was magnetically stirred for 48 h at 300 rpm at room temperature.

The surfaces of the GFRP laminate were manually abraded with sandpaper (grid 240). During this process, care was taken to not affect the fibres of the laminate. Before and after the roughening step, the GFRP surfaces were cleaned with a clean cloth soaked with isopropanol.

A manual applicator gun with a static-mixing nozzle was used to mix and apply the two-component epoxy paste adhesive, Araldite 2015. In order to have a correct mixture of both components, a small quantity of adhesive was first discarded. Small metallic spacers of 2 different thicknesses (approximately, 0.4 and 10.1 mm) were used to obtain a uniform adhesive bondline, as shown in Fig. 1. Two metallic strips and a sharp razor blade were used to build the spacers. These components were bonded by a fast curing adhesive. The razor blade was placed in between the metallic strips to create a pre-crack at the mid thickness of the bondline. The spacers were treated with a release agent before the bonding process. After the bonding process, the oven cure took place at 80 °C for 1 h according to manufacturer's specifications. After curing the specimens, the excess of adhesive on the sides was removed by abrasion. An even bondline thickness was obtained by making use of weights to uniformly compress the specimens during the curing process. The total thickness of the specimens was measured three times along the specimen length and the average was calculated in accordance with the ASTM D5528-13 [36]. The average bondline thickness was taken by subtracting the adherends' thickness.

2.2. Test set-up

The mode I fracture energy was evaluated from the DCB test. The DCB bonded joints were tested in a Zwick tensile test machine, equipped with a 20 kN load cell (precision of 0.5%). The displacement rate used was 1 mm/min and the tests were carried out to failure at laboratory conditions (temperature of 23 °C and relative humidity of 55%). At least four specimens were tested for every joint configuration and bondline thickness.

A thin layer of white paint was applied to the side of the specimens, and black speckles were painted on top, before any load was applied. The crack length was measured by means of a 3D image acquisition system placed at the side of the specimen. Pictures were acquired every second. The crack length was defined as the straight and horizontal line distance between the load line and the crack tip, where the load line is coincident with the centreline of the grips' pins. The displacement occurring in the end-blocks was considered negligible compared to the displacement of the arms of the specimens.

Fig. 3a shows an overview of the experimental test set-up, highlighting the mechanical extensometers (used to measure the total displacement of the specimen), the end-blocks and the 3D image acquisition system.

Four GFRP-GFRP and four steel-GFRP DCB bonded joints with thin adhesive layer were instrumented with stain gauges (Kyowa micro-measurements reference KFG-5-120-C1-11 and KFG-5-120-C1-23 with 120Ω nominal resistance for steel and GFRP adherends, respectively) to measure the adherends backface longitudinal strain. The strain gauges were bonded along the midline of the outer face of the adherends. In each specimen, the strain gauges were bonded at the same positions along the length direction in both adherends in order to assess the symmetry of the test. The distance between strain gauges from the applied force is: 1) GFRP-GFRP joints = {30, 60, 80, 100, 120 mm}; 2) steel-GFRP joints = {30, 60, 80, 100 mm}. Fig. 3b shows an instrumented GFRP-GFRP specimen being tested. Please note that solely the GFRP-GFRP and steel-GFRP bonded joints were instrumented with strain gauges because of their high complexity due to either the anisotropy of the GFRP adherends or the asymmetry of the bi-material joint, respectively.

2.3. Analysis of the fractured surfaces by a scanning microscope

All the fracture surfaces of the DCB joints were examined in a Keyence VR-3200 3D optical profiler. This device is composed of a three-dimensional measuring microscope and a fringe projection scanner. The scanner is characterized by <100 nm out-of-the plane resolution with up to a 200 × 200 mm^2 measuring area.

2.4. Attenuated total reflectance-Fourier transform infrared (ATR-FTIR)

The fracture surfaces of the representative bonded joints were analysed by the ATR-FTIR technique. The experiments were carried out by a PerkinElmer Spectrum 100 spectrometer equipped with the Universal ATR accessory. The spectrum was obtained by setting the accumulations required to 8 scans and the spectral range between 4000 and 600 cm^{-1} with a resolution of 4.0–7.99 cm^{-1}.

3. Data analysis: Penado-Kanninen model

Penado [37] developed a method to evaluate the compliance and the fracture energy of the DCB specimen with an adhesive layer by
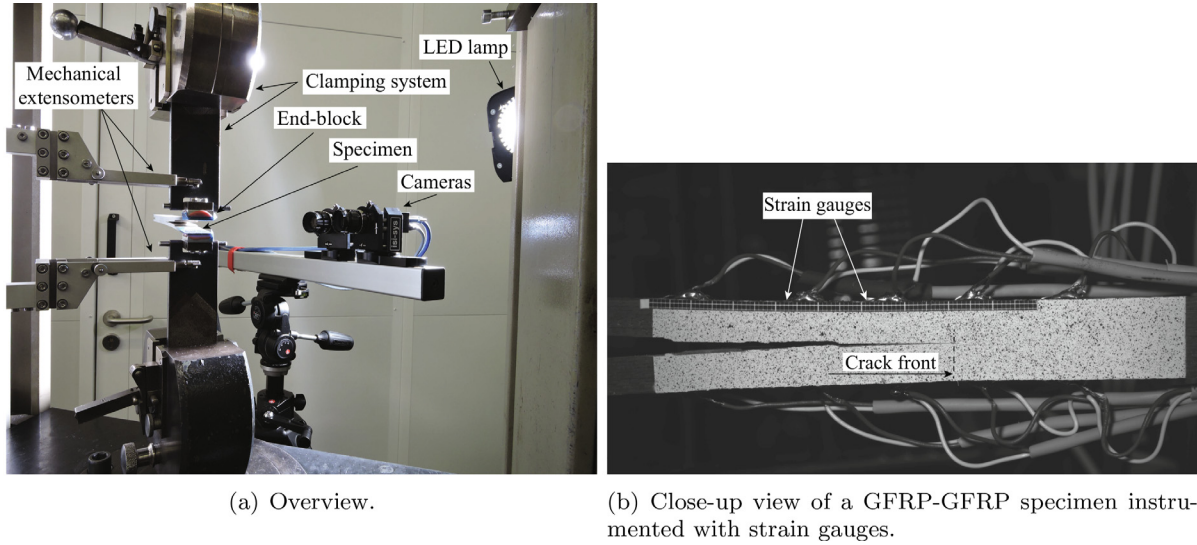
(a) Overview.

(b) Close-up view of a GFRP-GFRP specimen instrumented with strain gauges.

Fig. 3. Test set-up.

modifying the Kanninen's "augmented DCB model" [38] for crack propagation analysis of a homogeneous specimen. The Penado-Kanninen (PK) model is obtained by considering a finite length beam, which is partially free (representing the unbonded part of the specimen) and partially supported by an elastic foundation (representing the bonded region), see Fig. 4. The DCB specimen is assumed to be symmetric about the x-axis along the centreline of the adhesive layer. Only half of the specimen is represented in Fig. 4 (bondline of thickness t). The simplest theories are used: the Euler–Bernoulli beam theory and the Winkler foundation for the free and the bonded regions, respectively [39].

It should be noted that the Winkler correction for DCB specimens with softer and thicker interlayers was subject of the study of several researchers [38,40,41,37]. This approach remarkably allows the incorporation of the process zone at the crack tip. Indeed, the beams are not fixed at the crack tip due to the flexibility of the adhesive layer, which may lead to some vertical displacement of the beams within the bonded zone [42,43].

The solution of the displacement of the Penado-Kanninen beam model is given by,

$$w(x) = \frac{P}{6E_x^{f-adher}I\lambda^3} \begin{cases} (3a\lambda^3 x^2 - \lambda^3 x^3 + 6a\lambda^2 x + 3\lambda x + 3\lambda a + 3) & 0 \leqslant x \leqslant a \\ 3e^{\lambda x}[a\lambda\cos(\lambda x) + a\lambda\sin(\lambda x) + \cos(\lambda x)] & -\infty \leqslant x \leqslant 0 \end{cases} \tag{4}$$

$E_x^{f-adher}$ is the effective bending modulus of the adherend (in case of an isotropic adherend, $E_x^{f-adher} = E$; in case of an anisotropic adherend,

$E_x^{f-adher}$ is determined by the CLT), $I = \frac{Bh_{adherend}^3}{12}$ is the moment of inertia of the beam cross-section area, and λ is the wave number, the inverse of which defines the elastic process zone length. The process zone length, λ^{-1}, in the context of the elastic foundation is interpreted as the distance (from the crack tip) over which the positive peel stress is distributed. The λ^{-1} length exits beyond of the crack tip due to the finite rigidity of the adhesive. The λ is defined as,

$$\lambda = \sqrt[4]{\frac{k}{4E_x^{f-adher}I}}, \tag{5}$$

where k is the total foundation modulus describing the stiffness of the springs. It is assumed that the adhesive and the adherend act as springs in series. Therefore, assuming that k_{adher} and k_{adhes} represent the individual contributions, the total foundation modulus, k, is given by [37],

$$k = \frac{1}{\frac{1}{k_{adher}} + \frac{1}{k_{adhes}}}, \tag{6}$$

where

$$k_{adher} = \frac{4E_z^{adher}B}{h_{adher}}, \tag{7}$$

and

$$k_{adhes} = \left(\frac{E_a}{t}\right)B, \tag{8}$$

where E_z^{adher} is the adherend modulus in the z-direction (i.e., the out-of-plane tensile modulus), h_{adher} is the thickness of the adherend, E_a is the
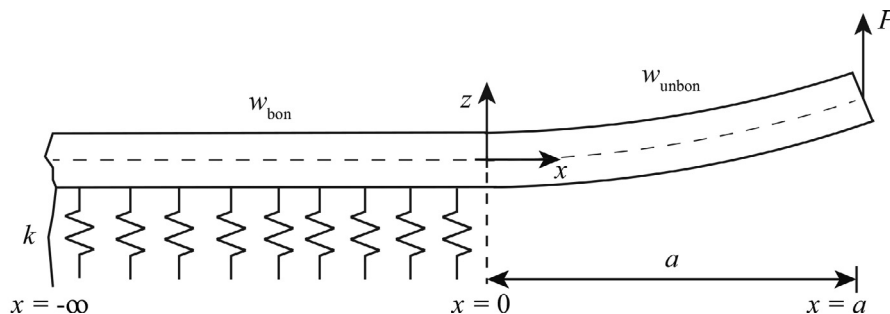

Fig. 4. DCB specimen modelled according to Penado-Kanninen model [39].

Young's modulus of the adhesive, t is half of the thickness of the adhesive layer, and B is the specimen width.

In the case of an isotropic adherend, $E_z^{adher} = E$. It should be noted that for a composite laminate composed of non-crimp fabric, as used in the present study, E_z^{adher} is dominated by the resin of the laminate, i.e., $E_z^{adher} \approx E_{yy}$ of a single UD-0° lamina.

The strain energy release rate is determined using the compliance method. The beam displacement at $x = a$ is given by,

$$\Delta = w_{unbon}(x = a) = \frac{P}{E_x^{f-adher} I \lambda^3} \left(\frac{1}{3} \lambda^3 a^3 + \lambda^2 a^2 + \lambda a + \frac{1}{2} \right). \quad (9)$$

Eq. 9 does not include the effect of the shear deformation in the unbonded part of the specimen. A correction for shear can be added,

$$\begin{aligned} \Delta &= w_{unbon}(x = a) \\ &= \frac{P}{E_x^{f-adher} I \lambda^3} \left(\frac{1}{3} \lambda^3 a^3 + \lambda^2 a^2 + \lambda a + \frac{1}{2} \right) + \frac{3Pa}{2BG_{xz}^{adher} h_{adher}}, \end{aligned} \quad (10)$$

where G_{xz}^{adher} is the shear modulus of the adherend in the xz-plane. For an isotropic adherend, $G = G_{xz}^{adher} = \frac{E}{2(1+\nu)}$, while for a composite material, the shear modulus G_{xz}^{adher} is estimated by using a smearing scheme. An example of a smearing scheme is the laminate homogenization method of Hyer and Knott [44].

The displacement given by Eq. 10 corresponds to half of the specimen. Therefore, for a single-material specimen, the total displacement is equal to 2Δ. The mode I strain energy release rate, G_{I-PK}, is then given by,

$$G_{I-PK} = \frac{P^2}{2B} \frac{dC}{da} = \frac{P^2}{BE_x^{f-adher} I \lambda^2} \left(\lambda^2 a^2 + 2\lambda a + 1 \right) + \frac{3P^2}{2B^2 G_{xz}^{adher} h_{adher}}, \quad (11)$$

where P is the applied load, C is the specimen compliance, B is the specimen width and da is the instantaneous crack length extension. A straight crack front is assumed. Eq. 11 seems of fundamental importance revealing an inherent effect of the adhesive thickness on the elastic process zone length, λ^{-1}. The mode I strain energy release rate is directly affected by the increase of the adhesive layer thickness.

3.1. Adaptation to bi-material bonded joints

As explained in sub-Section 2.1, the bi-material DCB bonded joints are designed by following the Strain based criterion [33] (see Eq. 1). This design criterion is achieved by matching the longitudinal strain distributions of the surfaces in contact with the adhesive layer. Therefore, the two adherends do not deform symmetrically and, thus, the total opening displacement is given by the sum of the displacement of each arm,

$$2\Delta_{bi-material} = w_{unbon}^{adher\ 1}(x = a) + w_{unbon}^{adher\ 2}(x = a). \quad (12)$$

The mode I strain energy release rate of the bi-material bonded joints, $G_{I-PK}^{bi-material}$, is then expressed as,

$$G_{I-PK}^{bi-material} = \frac{P^2}{2B} \left[\frac{\lambda_{adher1}^2 a^2 + 2\lambda_{adher\ 1} a + 1}{E_x^{f-adher\ 1} I_{adher\ 1} \lambda_{adher\ 1}^2} + \frac{3}{2BG_{xz}^{adher\ 1} h_{adher\ 1}} + \frac{\lambda_{adher\ 2}^2 a^2 + 2\lambda_{adher\ 2} a + 1}{E_x^{f-adher\ 2} I_{adher\ 2} \lambda_{adher\ 2}^2} + \frac{3}{2BG_{xz}^{adher\ 2} h_{adher\ 2}} \right]. \quad (13)$$

4. Results

4.1. Fracture surfaces

In Fig. 5, optical scans of the fracture surfaces of the representative specimens of all bonded joint types with a thin adhesive layer (of approximately 0.4 mm) are presented. These scans were taken from the fracture surfaces post-mortem with the Keyence VR-3200 3D optical profiler (see sub-Section 2.3). These bonded joints present unique features depending on the joint type. Looking at Fig. 5, the fracture surfaces of the representative:

- Steel-steel bonded joint show regions that are characterized by peaks and valleys, and regions with a smoother appearance, where the crack seems to propagate at the mid-thickness of the bondline (i.e., perfectly cohesive propagation), see Fig. 5a.
- GFRP-GFRP joint present some peaks and valleys as shown in Fig. 5b. Overall, the fracture surfaces reveal the tendency of the crack to grow closer to one of the adhesive-adherend interfaces, but within the adhesive. For example, in the representative specimen (see Fig. 5b), the crack propagated in the adhesive region nearby the interface with arm 2.
- Bi-material steel-GFRP bonded joint show rather different fracture features. These surfaces present "adhesive channels", which are noticeable in Fig. 5c, and regions where the crack jumps to planes distant from the mid-plane of the adhesive thickness. The stitching line of the GFRP laminate seems to have an influence on the development of the so-called "adhesive channels".

In Fig. 6, optical scans of the fracture surfaces of the representative specimens of all bonded joint types with a thick adhesive layer (of approximately 10.1 mm) are shown. Regardless of the bonded joint type, the crack has mostly propagated in an asymmetric manner (i.e., no geometric symmetry during crack growth). Two different trends are identified at the crack initiation locus:

- in all bonded joints with the initial pre-crack length, a_0, the failure initiation took place at an arbitrary plane close to one of the interfaces, but within the adhesive layer (see Fig. 6a). The mismatch in the stiffness of the materials at the interfaces (i.e., adherend and adhesive), leads to a peak of the stresses in this region of the specimen as reported by Bogy et al. and Goncalves et al. [3,45]. The higher the mismatch, the higher the stresses. In the bi-material bonded joints, the failure initiation took place nearby the steel adherend because the stiffness mismatch at the steel-adhesive interface is higher in comparison to the mismatch at the GFRP-adhesive interface. Overall, for longer crack lengths, the crack has propagated along the same plane, being the exception the steel-steel configuration. In steel-steel bonded joints, an alternating crack path within the adhesive layer was observed, although the crack did run closer to one interface than the other in some segments of the bonded regions (see Fig. 6a).
- in some cases, a_0 was extended, leading to failure initiation at the mid-plane of the adhesive layer (see Figs. 6c and 6b). However, as the crack propagated further, the crack jumped to the plane closer to one of the interfaces. In the bi-material bonded joints, the crack grew nearby the steel interface. The extension of the pre-crack length in some specimens is worthy of comment. This extension was an attempt to experimentally observe the effect of increasing pre-crack length. Indeed, an extension of a_0 forces the crack to stably propagate at the mid-thickness of the adhesive layer because the slope $\frac{dP}{d\Delta}$ decreases with increasing crack length [33]. However, the crack propagates in the same manner afterwards, travelling towards one of the interfaces.

#### 4.1.1. Attenuated total reflectance-Fourier transform infrared (ATR-FTIR) analysis

The fracture surfaces of the representative bonded joints were analysed by ATR-FTIR technique to evaluate the failure type (cohesive, adhesive failure or interlaminar in the GFRP adherend). The ATR-FTIR measurements performed on the fracture surfaces of the joints with the thicker adhesive layer were in agreement with the visual inspection, i.e., adhesive was found on both arms of the joints by naked eye. Concerning the joints with the thinner adhesive layer, there
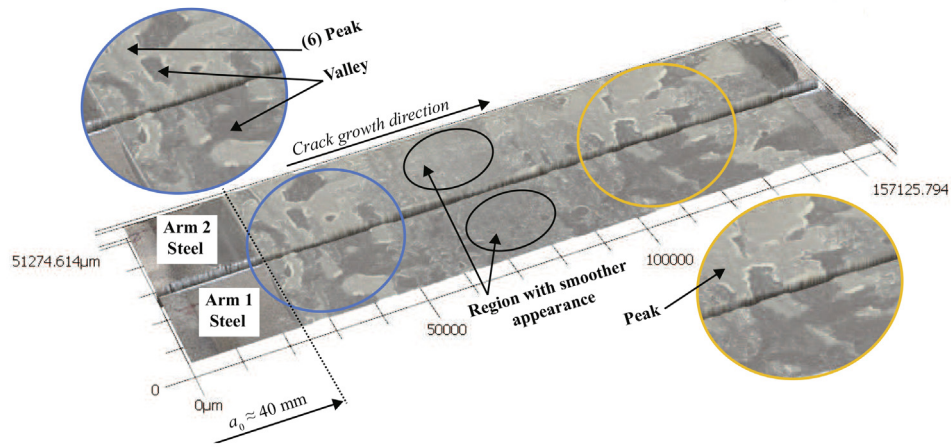
(a) Single-material steel-steel bonded joint.
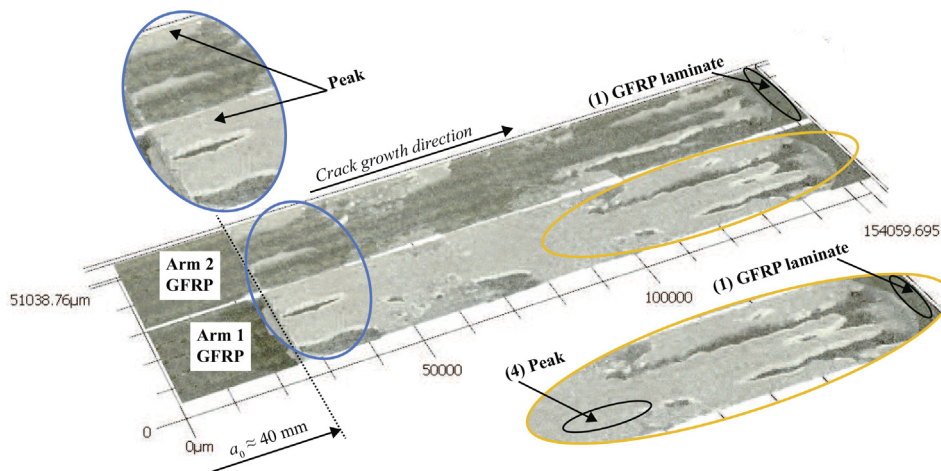
(b) Single-material GFRP-GFRP bonded joint.
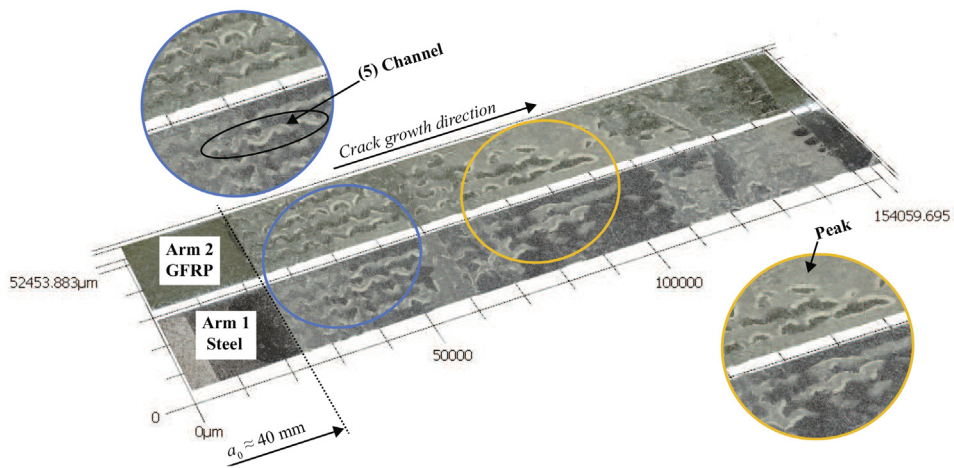
(c) Bi-material steel-GFRP bonded joint.

Fig. 5. Representative bonded joints with a thin adhesive layer: optical scans of the entire fracture surface of both adherends obtained by a scanning microscope.

was uncertainty regarding their failure type by visual inspection. However, the ATR-FTIR measurements show that the failure is cohesive regardless the bonded joint type. Therefore, the results of the joints with thinner bondline are presented and discussed in the subsequent paragraphs.

In all bonded joints with a thin adhesive layer, the ATR-FTIR measurements were performed on characteristic areas, such as peaks and "adhesive channels", where the crack propagated in a region remote from the mid-thickness plane. ATR-FTIR measurements were performed in six different areas: (1) sanded GFRP laminate (i.e., GFRP
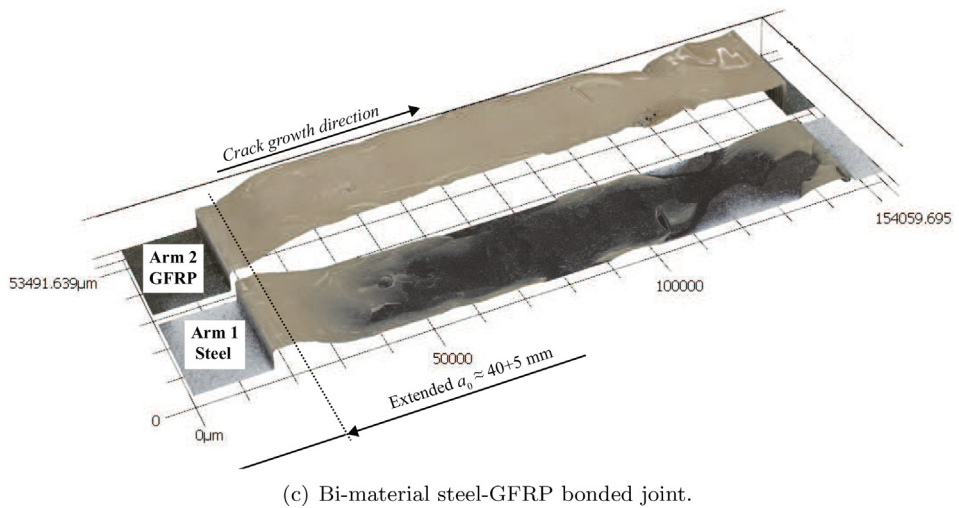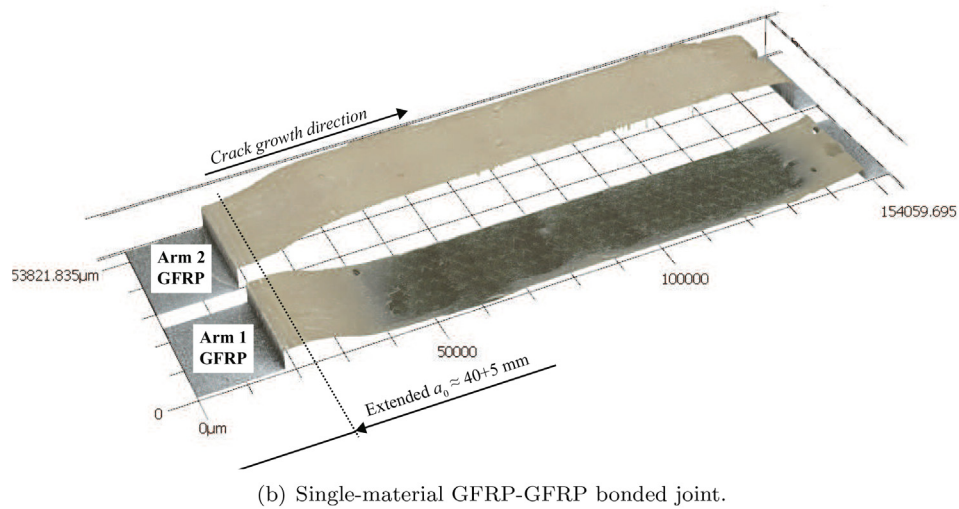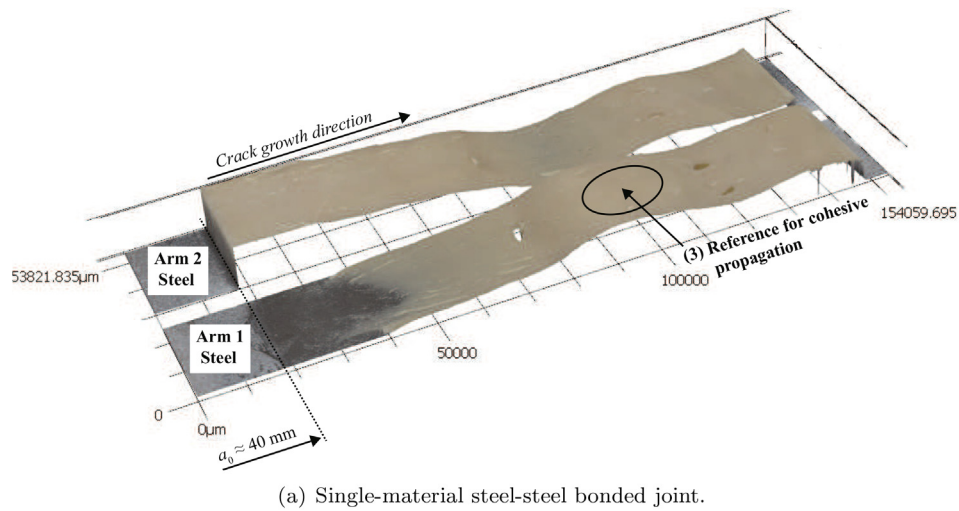
(a) Single-material steel-steel bonded joint.

(b) Single-material GFRP-GFRP bonded joint.

(c) Bi-material steel-GFRP bonded joint.

Fig. 6. Representative bonded joints with a thick adhesive layer: optical scans of the entire fracture surface of both adherends obtained by a scanning microscope.

laminate prior to bonding) – Reference 1 (Ref_1), (2) bulk adhesive (from a bulk adhesive plate cured at 80 °C during one hour) – Reference 2 (Ref_2), (3) fractured area of bare adhesive (area of cohesive propagation, i.e., the propagation took place within the adhesive layer) – Reference 3 (Ref_3), (4) fractured areas of the representative GFRP-GFRP bonded joint, (5) fractured areas of the representative steel-GFRP bonded joint, (6) fractured areas of the representative steel-steel bonded joint. Areas (1) and (4) are represented in Fig. 5b.

The areas analysed in the bi-material bonded joint are highlighted in Fig. 5c, while area (3) is represented in Fig. 6a. Finally, areas (6) are shown in Fig. 5a.

The ATR-FTIR spectra of the six analysed areas are shown in Fig. 7. A qualitative comparison is made. The spectra measured on areas (3–6) resemble the spectrum of the bulk adhesive, Ref_2. The similarity on the spectra is evidence of adhesive presence on the analysed fractured surfaces. The shape of the spectrum of the sanded GFRP laminate presents different peaks in comparison to the bulk adhesive spectrum, Ref_1 and Ref_2, respectively. The difference in the spectra is expected and is justified by the nature of the polymers studied. The GFRP laminate is composed of a rubber modified epoxy based vinyl ester resin, while Araldite 2015 is an epoxy adhesive.

Qin et al. [46] have conducted ATR-FTIR measurements on samples of bulk adhesive Araldite 2015. The spectra of the adhesive presented in this studied were qualitatively compared with the results of Qin et al. [46]. The same characteristic absorptions (peaks) were observed. The understanding of the functional groups associated with each absorption peak is distinct from the core objective of this paper, and hence the interested reader is referred to [46] for more details.

A closer look at the spectra is presented in Fig. 8. These results show the same absorption peaks for the adhesive reference samples, Ref_2 and Ref_3, and for the fracture surfaces of the bonded joints. The occurrence of those peaks in the fracture surfaces of the bonded joints with the thinner bondline is clear proof that adhesive has remained on them, indicating that cohesive propagation took place.

Finally, the spectrum of the sanded GFRP laminate (Ref_1) stands out from the other spectra (see Fig. 8, specially in the wavenumbers range of 1850–500 cm^{-1} (Fig. 8). The differences in the spectra are indicative of the presence of different types of materials. As none of the fractured surfaces presented resemblances with Ref_1, it is therefore concluded that crack propagation in the GFRP laminate has not occurred.

4.2. Load–displacement curves and PK model validation

Figs. 9 and 10 show the representative load–displacement curves of the single-material steel-steel and the bi-material steel-GFRP bonded joints with a thin (approximately 0.4 mm) and thick adhesive layer (approximately 10.1 mm), respectively. Only the representative curves are presented as the experimental load–displacement curves are consistent for each specimen within the same test series. Figs. 9 and 10 also present the theoretical estimations of the load–displacement curves based on the PK model.

The experimental displacement was predicted by the Penado-Kanninen model. Eq. 10 is used to estimate the displacement of the single-material DCB configurations (please note that the total displacement is equal to 2Δ), while Eq. 12 is used for the bi-material DCB configuration. The displacement is calculated for each data set: experimental load P_i and visually measured crack length a_i, where i is the number of data points available for each specimen (black dots on top of the experimental load–displacement curves in Figs. 9 and 10). The mid-adhesive thickness, t, is used as an input to predict the displacement, see *PK: crack growth at mid-adhesive layer* results in Figs. 9 and 10. For the bonded joints with a thick adhesive layer, the real crack growth path is also used as an input in the PK model. The model is updated for each point to capture the alternating crack path observed in these joints, leading to a better approximation of the real case. For each a_i, the average adhesive thickness along the specimen width is used in the PK model, see *PK: real crack growth path* results in Fig. 10. The results concerning the GFRP-GFRP configuration are not presented in this paper, as the trend of the theoretical estimations is similar to the one found on the steel-steel configuration regardless the bondline thickness.

Looking at the bonded joints with the thinner bondline (Fig. 9), good agreement is observed between the experimental and the theoretical estimations based on the PK model, though no perfectly cohesive propagation occurred (the crack locus deviated from the adhesive layer mid-thickness). These results show that the changes in the crack locus direction seem to not significantly affect the plastic zone ahead of the crack tip. As the bondline is thin, the development of this zone is controlled by the physical constraint from the adherends [5–13].

The trend between the experimental and the theoretical results is rather different in the bonded joints with the thicker bondline (Fig. 10). Although the model gives an approximation of the overall form of the load–displacement curves, that approximation is in general an overestimation of the experimental results. The analysis of the theoretical results should be divided in two groups: initial propagation region (approximately up to 3 mm of displacement), and further away propagation region (displacement higher than 3 mm). In the initial propagation region, the PK model resembles the experimental case
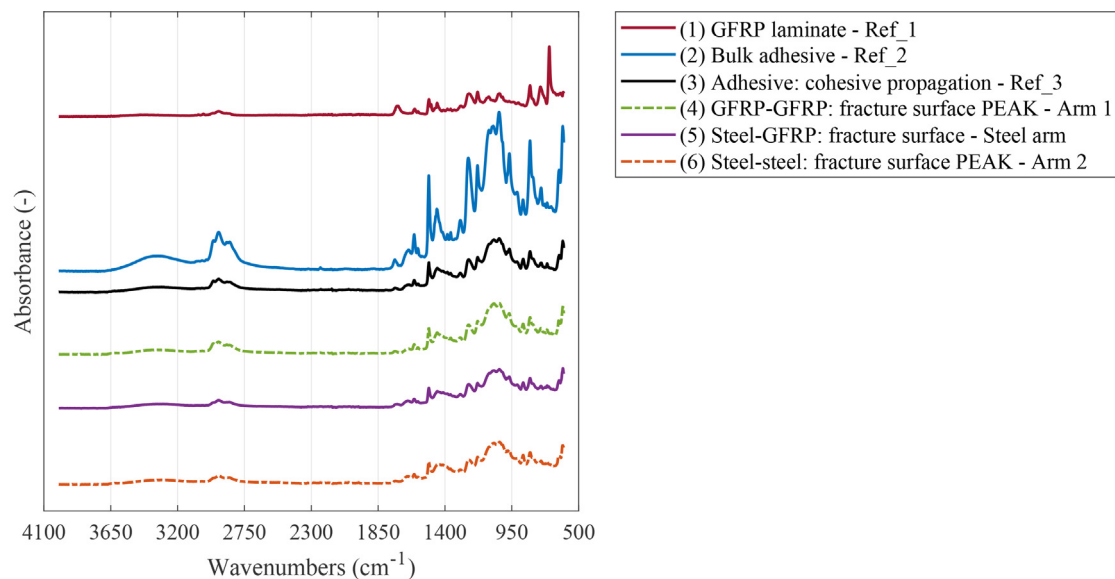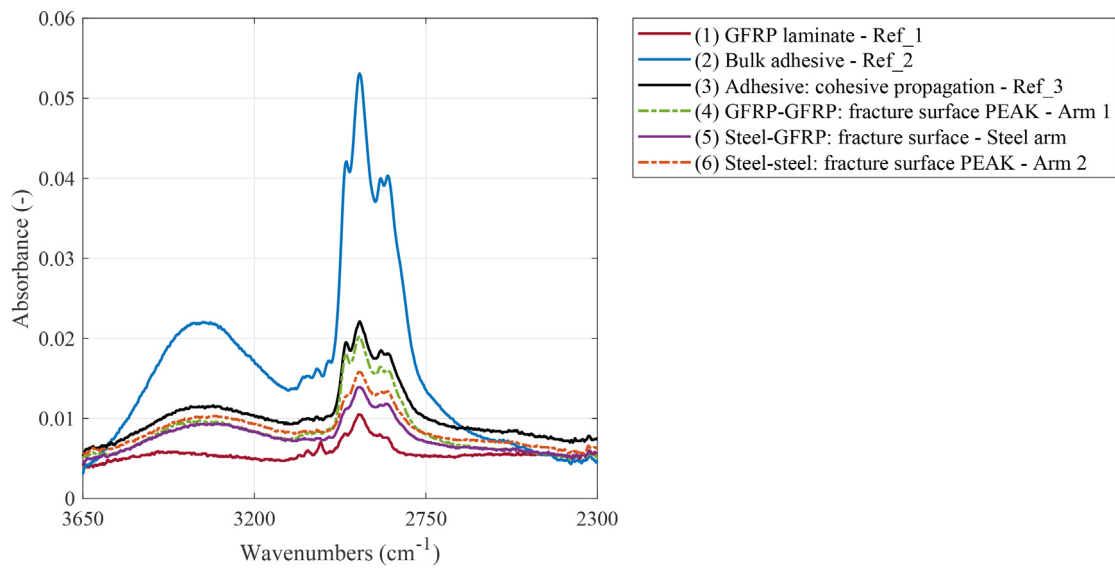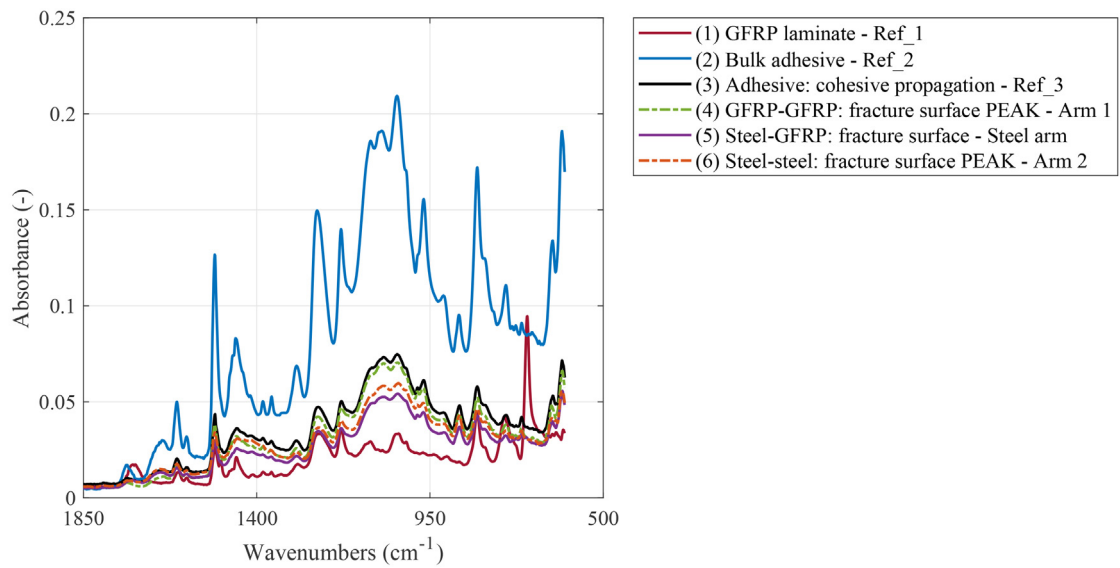

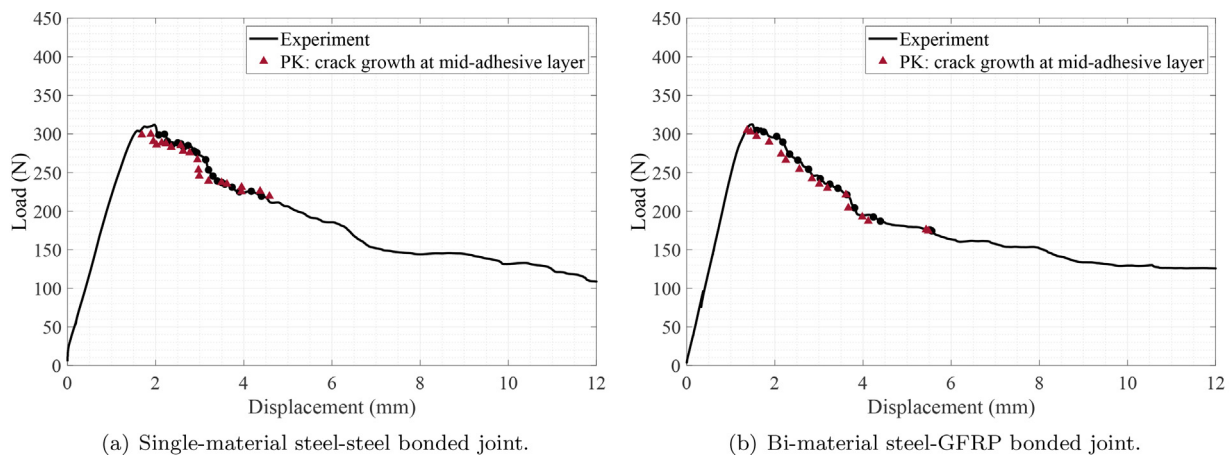**Fig. 7.** ATR-FTIR spectra: qualitative comparison.

(a) Close-up iof the wavenumbers in the range of 3650-2300 cm^{-1}.

(b) Close-up of the wavenumbers in the range of 1850-500 cm^{-1}.

Fig. 8. ATR-FTIR spectra.

(a) Single-material steel-steel bonded joint.

(b) Bi-material steel-GFRP bonded joint.

Fig. 9. Representative bonded joints with thin adhesive layer: load–displacement curves.

(a) Single-material steel-steel bonded joint.

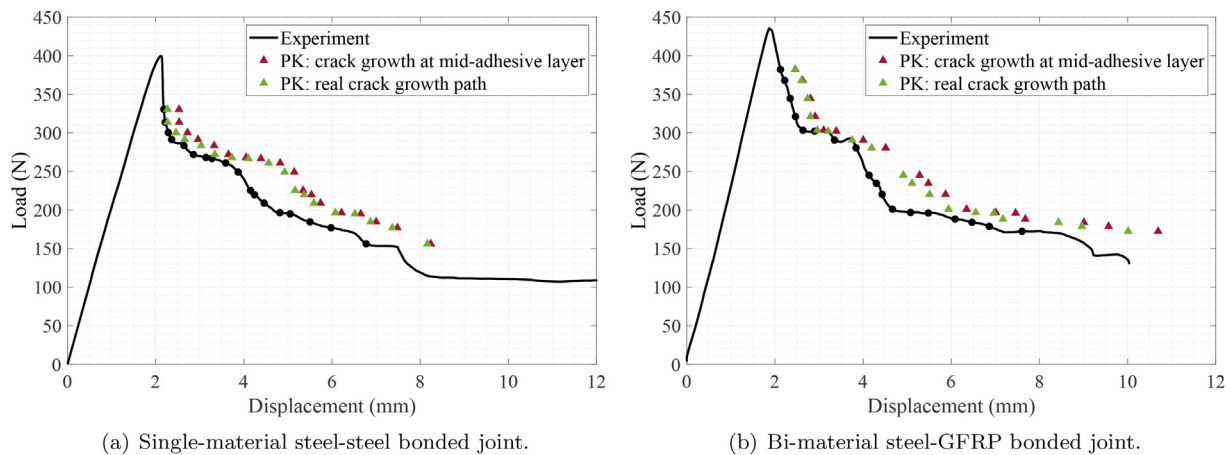(b) Bi-material steel-GFRP bonded joint.

Fig. 10. Representative bonded joints with thick adhesive layer: load–displacement curves.

as there is no adhesive in the unbonded part of the specimen. Therefore, good agreement between the experimental and theoretical results is obtained. By considering the real crack path, the theoretical results are more accurate as the contribution of the adhesive to the opening displacement of the specimen is properly determined. However, in the further away propagation region, the stiffness of the adhesive layer in the unbonded part of the specimen (i.e., in the cracked portion of the specimen) is not included in the model. The bending stiffness of the specimen is thus underestimated, resulting in higher theoretical displacement. Moreover, the alternating crack path gives an indication that the propagation occurred most likely under mixed mode conditions as shown in [47], which is not accounted in the model.

As previously described in Section 3, in the PK model the process zone at the crack tip is not disregarded. The flexibility of the adhesive at the crack tip is accounted for the specimen displacement, which implies that the geometric (such as the bondline thickness) and mechanical properties (such as the adhesive Young's modulus) of the adhesive are used as parameters of the model. The reasonably good theoretical results, even though the visually measured crack length is used as input, shown in Figs. 9 and 10, show the relevance of the PK model to address the mode I fracture behaviour of bonded joints. Therefore, the PK model is used to calculate the mode I strain energy release rate of the investigated bonded joints. The failure is assumed to be perfectly cohesive, i.e., at the mid-thickness of the adhesive layer.

4.3. Resistance-curves

Figs. 11 and 12 present the *Resistance*-curves of the representative specimens of the steel-steel and steel-GFRP bonded joint types with thin and thick adhesive layers, respectively. For each representative *Resistance*-curve, the longitudinal and transverse crack path profiles are shown in the length and width directions. These crack path profiles are taken from the 3D optical scans at specific locations at the specimen width, $B' = \{5, 12.5, 20 \text{ mm}\}$, and at arbitrary crack lengths, $\{a_1, a_2, a_3\}$.

G_I of the single-material DCB configurations is calculated by Eq. 11, while Eq. 13 is used to calculate the mode I strain energy release rate of the bi-material DCB configuration. G_I is calculated for each data set: experimental load P_i and visually measured crack length a_i, where i is the number of data points available for each specimen. Both longitudinal and transverse crack path profiles in Figs. 11 and 12 show that the crack did not grow uniformly along the specimen width, regardless the bonded joint type and adhesive layer thickness. Therefore, the failure surfaces are not symmetric along the width, which makes it difficult to accurately identify the crack tip position and to determine the crack length.

The *Resistance*-curves show the evolution of the mode I strain energy release rate, G_I, as a function of the visually measured crack length. These curves are characterized by an oscillatory behaviour around a mean G_I value. In fact, the crack path profiles in Figs. 11 and 12 show that the crack did not always propagate along the same adhesive height, regardless of the joint configuration and the adhesive bondline thickness. The changes in the crack path position lead to alternating crack paths, which result in experimental load–displacement curves characterized by a non-smooth behaviour as shown in Figs. 9 and 10. The non-smooth behaviour indicates that the crack locus direction has changed several times during the crack growth process, potentially affecting the plastic zone (size and shape), forming ahead of the crack tip. As energy dissipation mainly occurs in the plastic zone, no steady-state, self-similar regime in the *Resistance*-curves is expected, as it is corroborated by Figs. 11 and 12. Therefore, G_I is not constant throughout the crack growth process.

Moreover, the overall trend of the *R*-curves of the joints with thin adhesive bondline is as expected, and while the value seems to increase during the crack growth, such could be treated as inherent property of the DCB as shown in [48].

## 5. Mode I fracture energy results and Discussion

In Fig. 13, the mode I strain energy release rate is plotted against the adhesive bondline thickness. The results of the three studied configurations are shown: steel-steel, GFRP-GFRP, and steel-GFRP. The maximum, Δ, and minimum, $\triangledown$, values of G_I of every specimen are plotted against the average thickness of the corresponding bondline. For each bonded joint type and nominal bondline thickness, two error bars are shown, representing the scatter of the bondline thickness and G_I results. The mode I fracture energy, G_{Ic}, is given by ● and corresponds to the mean of all G_I points (maximum and minimum) and it is plotted against the average bondline thickness of each bonded joint type. Table 4 gathers the minimum, maximum as well as the average values of the bondline thickness and mode I fracture energy, G_{Ic}, of all bonded joint types.

The results in Fig. 13 and Table 4 show that, for this set of bonded joints and bondline thicknesses, the mode I fracture energy is globally independent of the adherend material, even though the fracture surfaces are different. Concerning the joints with the thinner adhesive bondline, G_{Ic} varies between 0.60 and 0.72 N/mm, being the lower limit given by the GFRP-GFRP and steel-GFRP configurations and the upper limit given by the steel-steel configuration. Concerning the bonded joints with the thicker adhesive bondline, G_{Ic} varies between 0.90 and 1.10 N/mm, being the lower limit given by the steel-GFRP configuration and the upper limit given by the GFRP-GFRP and steel-steel configurations.
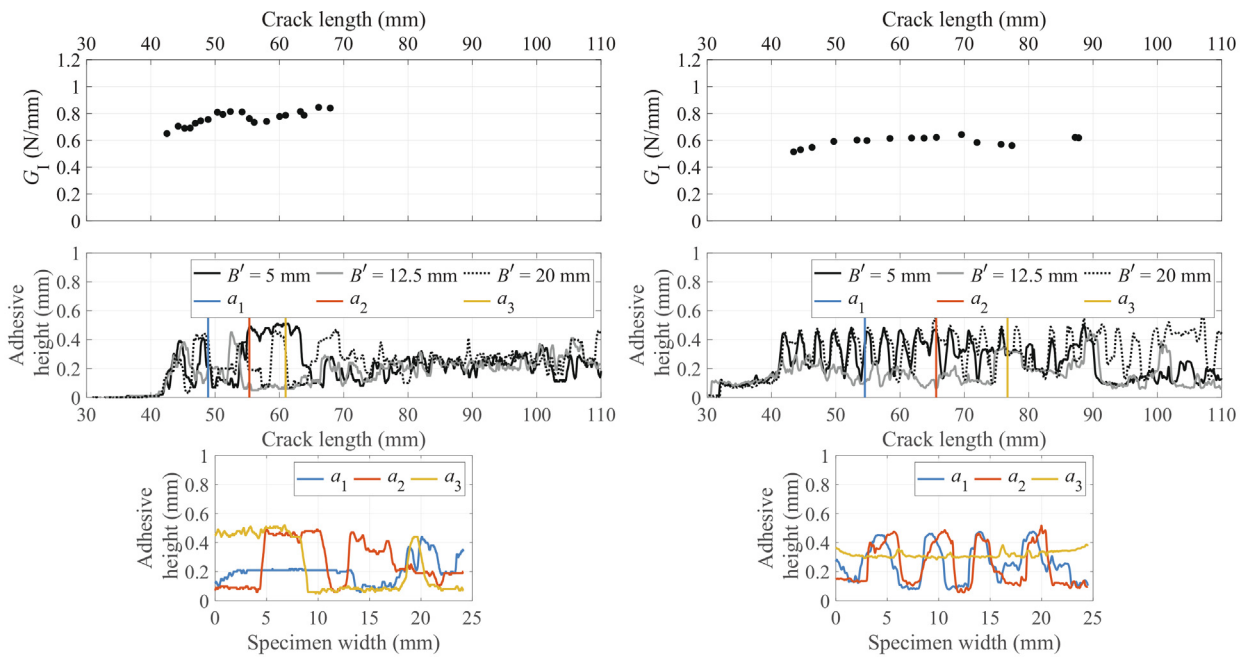
(a) Single-material steel-steel bonded joint. The adhesive height profiles are taken from Arm 1 shown in Fig. 5(a).

(b) Bi-material steel-GFRP bonded joint. The adhesive height profiles are taken from Arm 1 shown in Fig. 5(c).

Fig. 11. Representative bonded joints with thin adhesive layer: *Resistance*-curves and height of adhesive remaining in one of the fracture surfaces (the crack length measurements correspond to data gathered from the image acquisition system).
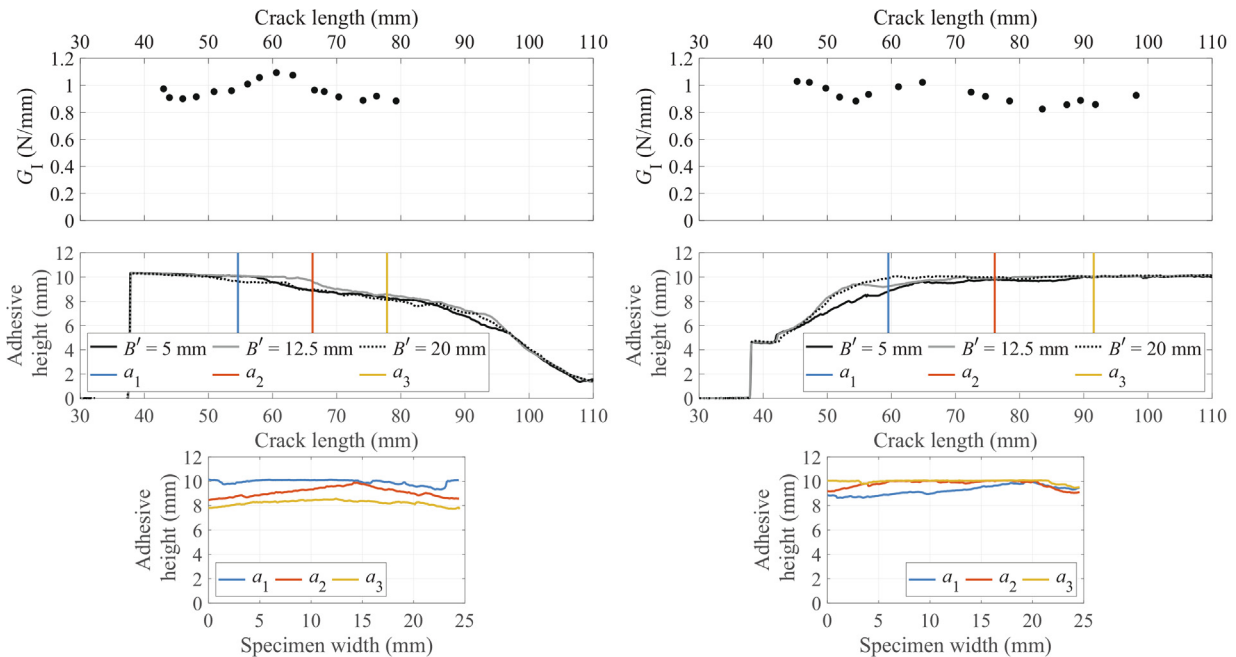
(a) Single-material steel-steel bonded joint. The adhesive height profiles are taken from Arm 2 shown in Fig. 6(a).

(b) Bi-material steel-GFRP bonded joint. The adhesive height profiles are taken from Arm 2 shown in Fig. 6(c).

Fig. 12. Representative bonded joints with thick adhesive layer: *Resistance*-curves and height of adhesive remaining in one of the fracture surfaces (the crack length measurements correspond to data gathered from the image acquisition system).

In order to better understand the independence of G_{Ic} on the adherend material, the region ahead of the crack tip ($-\infty \leqslant x \leqslant 0$) is analytically and experimentally analysed as shown in Fig. 14. More specifically, Fig. 14a shows the displacement of the PK model in the bonded region, w_{bon} from Eq. 4, of the single-material bonded joints

with thin and thick adhesive layers. Cohesive propagation at the mid-thickness of the bondline is assumed. One representative curve is shown in Fig. 14a for each bonded joint type and bondline thickness. Fig. 14b presents representative experimental results for normalised longitudinal strain, ε_{xx}, of instrumented GFRP-GFRP and steel-GFRP
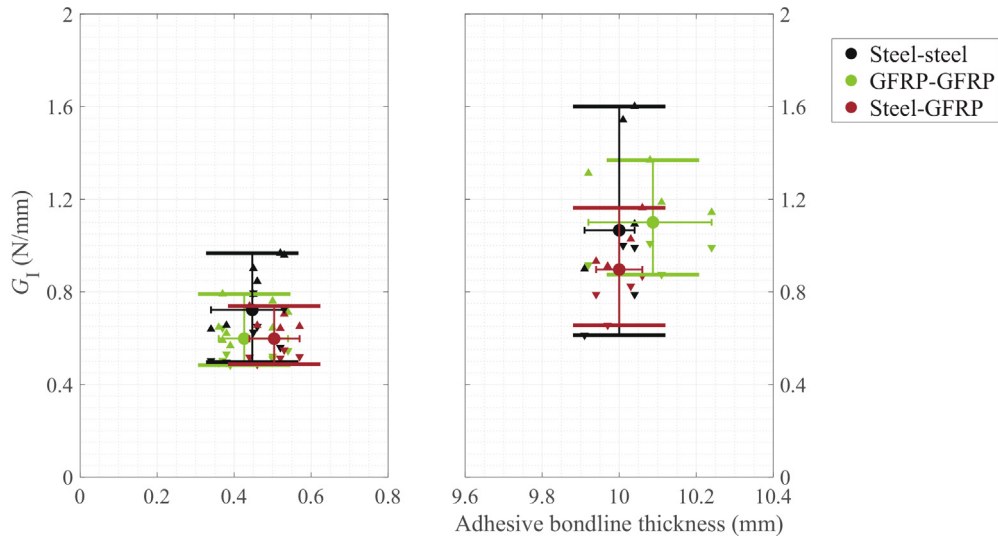
Fig. 13. Mode I strain energy release rate *vs.* adhesive bondline thickness for all bonded joint types.

Table 4
Minimum, average and maximum values of the bondline thickness (in mm) and the mode I fracture energy, G_{Ic}, (in N/mm) for all studied bonded joints.

Bondline	Thin			Thick		
Joint type	GFRP-GFRP	Steel-steel	Steel-GFRP	GFRP-GFRP	Steel-steel	Steel-GFRP
$2t_{min}$	0.36	0.34	0.44	9.92	9.91	9.94
$2t_{av.}$	0.43	0.45	0.50	10.09	10.00	10.00
$2t_{max}$	0.54	0.53	0.57	10.24	10.04	10.06
G_{Imin}	0.48	0.50	0.49	0.88	0.61	0.66
$G_{Iav.}$	0.60	0.72	0.60	1.10	1.07	0.90
G_{Imax}	0.79	0.97	0.74	1.37	1.60	1.16

DCB joints. ε_{xx} is normalised by the instantaneous applied force, P, and by the strain gauges position, $a_{straingauge}$. The x axis is shifted to superimpose the experimental curves. Please note that the experimental results are from strain gauges placed at the same position in both adherends (i.e., Arm 1 or Arm 2). The analytical solutions are derived from,
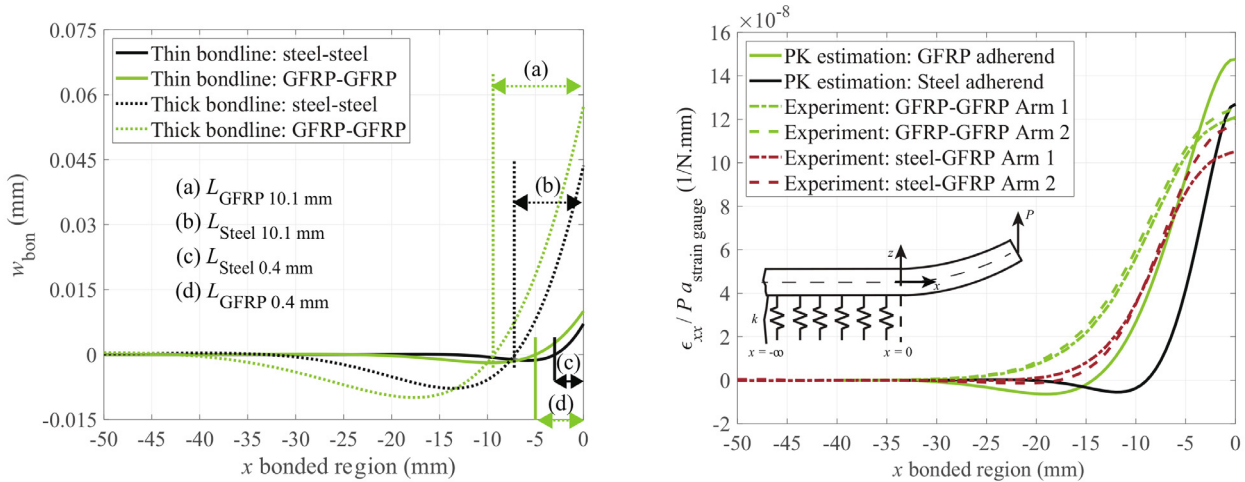
(a) Displacement of PK model in the bonded region, Eq. 4.

(b) Experimental results and analytical solutions for normalised longitudinal strain, ϵ_{xx}, of instrumented DCB joints.

Fig. 14. Analysis of the region ahead of the crack tip ($-\infty \leqslant x \leqslant 0$): analytical approach – via PK model, and experimental approach – via strain gauges bonded in the outer face of the adherends.

$$\frac{\varepsilon_{xx}}{Pa_{\text{straingauge}}} = \frac{h_{\text{adherend}}}{2Pa_{\text{straingauge}}} \frac{d^2w}{dx^2} \text{ for } -\infty \leqslant x \leqslant 0. \quad (14)$$

The length of the plastic region was estimated in a previous study from the authors [13] and is approximately 1 mm, considering plane strain conditions. This means that the two bondline thicknesses considered lay in two different regions: the theoretical estimated plastic region is larger than the thin bondline, but smaller than the thick bondline. Therefore, the physical constraint of the adherends is higher in the thin adhesive layer rather than in the thick one, resulting in different crack paths and fracture surfaces as shown in Figs. 11,12 and 5 and 6, respectively.

In Fig. 14a, the segments of the curves with positive values of w_{bon} are highlighted and labelled as $L_{\text{GFRPorSteel,0.4or10.1 mm}}$, depending on the adherend material and the bondline thickness of the bonded joint. $L_{\text{GFRPorSteel,0.4or10.1 mm}}$ provides a length scale of the portion of the adhesive in the bonded region that is being deformed: part of the adhesive within the length $L_{\text{GFRP or Steel, 0.4 or 10.1 mm}}$ is in the plastic regime, while the other fraction is in the elastic regime. Regardless the bondline thickness, higher values of w_{bonGFRP} and L_{GFRP} than $w_{\text{bon Steel}}$ and L_{Steel} are seen in Fig. 14a. The low E_z^{GFRP} results in higher flexibility at the crack tip (see Eqs. (6)–(8)), which explains the higher $w_{\text{bon GFRP}}$ in the bonded region for GFRP adherends in comparison with steel adherends. In addition, the high bending stiffness of the GFRP adherend results in positive $w_{\text{bon GFRP}}$ extended along a larger distance ahead of the crack tip. A similar observation on the effect of the bending stiffness on the extent of length L was made in [5].

The experimental results in Fig. 14b show that the process zone is clearly evidenced by the strain gauges bonded in the outer face of the adherends. For each bonded joint type, when comparing the normalised strain of two gauges that are bonded to the upper adherend and to the lower one, good superimposition of normalised strain in the bonded part is found. This is an indication of the symmetry of the tests, i.e., both adherends could uniformly deform in the longitudinal direction, resulting in pure mode I loading conditions. Moreover, the normalised strain results of the GFRP-GFRP joint are higher than the steel-GFRP results in the entire extent of the bonded region, which is in accordance with the analytical results shown in Fig. 14a. Concerning the normalised strain, the steel-steel configuration is expected to appear close to the lower bound of the steel-GFRP experimental results. Finally, the PK estimation follows the tendency of the experimental curves, regardless of the adherend material. However, the region near to the crack tip, $x = 0$, is overestimated, while the extension of the positive part of the normalised strain curves is underestimated. It should be noted that the adhesive is elastically modelled, while in reality part of the adhesive in the region ahead of the crack tip is in the plastic regime. In fact, if a tangential modulus, approximately one quarter of the initial linear modulus of the adhesive, would be consider, the analytical results of the normalised strain would get closer to the experimental ones. The stress–strain curve of the adhesive is shown in a previous study from the authors [13].

The high bending stiffness of the adherends, due to either the high stiffness of the steel or the relatively thick GFRP laminate, created similar constraint degree in the adhesive. This is demonstrated by the experimental normalised strain curves present in Fig. 14b. Indeed, the intensity of the normalised strain is of the same magnitude regardless of the adherend material. Therefore, it can be concluded that the constraint imposed by the adherends to the adhesive is the same. It has been proved by other researchers [10] that the intensity of plasticity ahead of the crack tip is more important than the extension of adhesive undertaking deformation for the fracture energy. By having a plastic region length of 1 mm, only a small portion of the segment L near $x = 0$ is in fact in the plastic regime. As energy dissipation mainly occurs in this region and as the intensity of the normalised strain is similar regardless the joint type, similar values of the mode I fracture energy should be expected.

Several researchers [5–12] have shown that the constraint effect of the adherends decreases with increasing bondline thickness, in case of cohesive propagation. In fact, this can be shown by the analytical results present in Fig. 14a. The ratio $\frac{L_{\text{GFRP}}}{L_{\text{Steel}}}$ was determined for both bondline thicknesses. This ratio gives an indication of the effect of the adherend material on the length L for each bondline thickness. It is interesting to notice that, for the thinner bondline, $\frac{L_{\text{GFRP}}}{L_{\text{Steel}}}$ is equal to 183%, whilst for the thicker bondline a ratio of 138% is obtained. By increasing the bondline thickness (from 0.4 mm to 10.1 mm), there is a reduction of almost 50% of the ratio $\frac{L_{\text{GFRP}}}{L_{\text{Steel}}}$.

Nevertheless, in the experiments of the joints with thick adhesive layer (of approximately 10.1 mm), the crack propagated asymmetrically regardless of the joint type. As explained in sub-Section 4.1, the asymmetric propagation occurred either along a remote plane from the mid-adhesive thickness, or in an alternating way within the bondline, although closer to one interface than the other in some segments of the bonded areas (see Fig. 6). Although the propagation was asymmetric, overlapping values of the mode I fracture energy were found, as shown in Fig. 13. Overall, it seems that the adhesive could deform similarly in the joints with the thick bondline, although the crack has been constrained in one side by different types of adherends (i.e., either by a steel- or GFRP-adherend).

As mentioned in sub-Section 4.1, in the GFRP-GFRP and bi-material steel-GFRP bonded joints, the crack grew close to one of the adhesive-adherend interfaces, but within the adhesive layer (see Figs. 6b and 6c). In the bi-material case, that interface was the adhesive-steel one due to the higher stiffness mismatch between the adhesive layer and the steel adherend. The higher the stiffness mismatch of the materials in the region of the interface, the higher the local stresses [3,45], which leads to faster crack propagation and, thus, to lower fracture energy. Therefore, the lower range of G_I values of the steel-GFRP joints in comparison with the GFRP-GFRP joints is related with the crack growth location within the bondline. The fracture of the GFRP-GFRP and the bi-material joints with thick adhesive layer was similar in all specimens, resulting in a small range of G_I values (see Fig. 13). In the steel-steel joints, the trend of fracture was rather different. Although the crack grew closer to one interface than the other, an alternating crack path behaviour was observed. This means that the crack travelled during the test from one interface to the other. The energy needed for crack propagation in a region close to the interface or in the bulk adhesive is different, resulting in the larger range of G_I values found in Fig. 13.

6. Concluding remarks

The primary objective of this study was to investigate the effect of the material of the adherends on the mode I fracture behaviour of bonded joints. Single-material (i.e., steel-steel and GFRP-GFRP) and bi-material (i.e., steel-GFRP) joints bonded with a structural epoxy adhesive were tested under DCB fracture test conditions. Moreover, two different adhesive bondline thicknesses were considered: 0.4 mm (thin bondline) and 10.1 mm (thick bondline). Some specimens were instrumented with strain gauges to assess the crack growth process. The Penado-Kanninen (PK) reduction scheme was outlined and applied to evaluate the mode I strain energy release rate, G_I. The morphology of the fractured surfaces was examined by a 3D optical profiler and their chemical composition was analysed by ATR-FTIR technique.

The failure was cohesive in all bonded joints. Overall, the fracture surfaces of the joints with the thinner adhesive layer were characterized by peaks and valleys, revealing a non-smooth crack propagation. Asymmetric crack growth (i.e., no geometric symmetry during crack growth) always occurred on the thicker bonded joints. By assuming perfectly cohesive propagation (i.e., at the mid-thickness of the adhesive layer), the PK model appeared to be suitable to predict the exper-

imental displacement of the thinner bonded joints, regardless the bonded joint type. For the joints with thick bondline, the PK model provided a reasonable approximation of the experimental load–displacement curve, even though the crack propagated asymmetrically. An improvement on the theoretical estimations was obtained when considering the real crack path as an input in the model.

The mode I fracture energy, G_{Ic}, showed to be independent of the adherend type and joint configuration (i.e., single- or bi-material). For the joints with a thin adhesive layer, G_{Ic} presented average values between 0.60 and 0.72 N/mm, while for the bonded joints with a thick adhesive layer average values between 0.90 and 1.10 N/mm were determined. In the joints with a thin adhesive layer, the results from the strain gauges revealed a similar degree of constraint imposed to the adhesive by the high-modulus (i.e., steel) and/or relatively thick (i.e., composite) adherends. The similar constraint degree contributed to a similar strain field in the plastic region and, therefore, to similar G_{Ic} values for all joint configurations with a thin adhesive layer. In all bonded joints with a thick adhesive layer, the crack grew within the adhesive but closer to the adhesive-adherend interface with the highest stiffness mismatch. In the bi-material bonded joints, the crack grew nearby the region of the adhesive-steel interface. The similar results of the mode I fracture energy showed that the adhesive could deform similarly, although the crack has been constrained in one side by different types of adherends (i.e., either by a steel- or GFRP-adherend).

Declaration of Competing Interest

The authors declare that they have no known competing financial interests or personal relationships that could have appeared to influence the work reported in this paper.

Acknowledgements

References

[1] Seong MS, Kim TH, Nguyen KH, Kweon JH, Choi JH. A parametric study on the failure of bonded single-lap joints of carbon composite and aluminum. Compos. Struct. 2008;86(1–3):135–45. https://doi.org/10.1016/j.compstruct.2008.03.026.

[2] International Association of Classification Societies, No. 47 Shipbuilding and Repair Quality Standard (Rev. 7 June 2013), Tech. Rep. 1996 (2013)..

[3] Bogy DB. On the problem of edge-bonded elastic quarter-planes loaded at the boundary. Int. J. Solids Struct. 1970;6(9):1287–313. https://doi.org/10.1016/0020-7683(70)90104-6.

[4] de Moura MFSF, Campilho RDSG, Gonçalves JPM. Crack equivalent concept applied to the fracture characterization of bonded joints under pure mode I loading. Compos. Sci. Technol. 2008;68:2224–30. https://doi.org/10.1016/j.compscitech.2008.04.003.

[5] Wang SS, Mandell JF, McGarry FJ. An analysis of the crack tip stress field in DCB adhesive fracture specimens. Int. J. Fract. 1978;14:39–58. https://doi.org/10.1007/BF00032383.

[6] Kinloch AJ, Shaw SJ. The fracture resistance of a toughened epoxy adhesive. J. Adhes. 1981;12:59–77. https://doi.org/10.1080/00218468108071189.

[7] Hunston DL, Kinloch AJ, Wang SS. Micromechanics of fracture in structural adhesive bonds. J. Adhes. 1989;28:103–14. https://doi.org/10.1080/00218468908030877. http://www.tandfonline.com/doi/abs/10.1080/00218468908030877.

[8] Daghyani HR, Ye L, Mai YW. Mode-I fracture behaviour of adhesive joints. Part I. Relationship between fracture energy and bond thickness. J. Adhes. 1995;53 (3–4):149–62. https://doi.org/10.1080/00218469508009935.

[9] Daghyani HR, Ye L, Mai YW. Mode-I fracture behaviour of adhesive joints. Part II. Stress analysis and constraint parameters. J. Adhes. 1995;53(3–4):163–72. https://doi.org/10.1080/00218469508009936.

[10] Cooper V, Ivankovic A, Karac A, McAuliffe D, Murphy N. Effects of bond gap thickness on the fracture of nano-toughened epoxy adhesive joints. Polymer 2012;53(24):5540–53. https://doi.org/10.1016/j.polymer.2012.09.049.

[11] Ranade SR, Guan Y, Ohanehi DC, Dillard JG, Batra RC, Dillard DA. A tapered bondline thickness double cantilever beam (DCB) specimen geometry for combinatorial fracture studies of adhesive bonds. Int. J. Adhes. Adhes. 2014;55:155–60. https://doi.org/10.1016/j.ijadhadh.2014.08.006.

[12] K.J. Maloney, Micro-architected Adhesive Joints, Ph.D. thesis, University of Cambridge, 2016..

[13] Lopes Fernandes R, Teixeira de Freitas S, Budzik MK, Poulis JA, Benedictus R. From thin to extra-thick adhesive layer thicknesses: fracture of bonded joints under mode I loading conditions. Eng. Fract. Mech. 2019;218(106607):1–22.

[14] Evans AG, Dalgleish BJ, He M, Hutchinson JW. On crack path selection and the interface fracture energy in bimaterial systems. Acta Metall. 1989;37 (12):3249–54. https://doi.org/10.1016/0001-6160(89)90197-1.

[15] Fleck NA, Hutchinson JW, Zhigang S. Crack path selection in a brittle adhesive layer. Int. J. Solids Struct. 1991;27(13):1683–703. https://doi.org/10.1016/0020-7683(91)90069-R.

[16] Chen B, Dillard DA. Numerical analysis of directionally unstable crack propagation in adhesively bonded joints. Int. J. Solids Struct. 2001;38(38–39):6907–24. https://doi.org/10.1016/S0020-7683(01)00006-3.

[17] Chen B, Dillard DA. The effect of the T-stress on crack path selection in adhesively bonded joints. Int. J. Adhes. Adhes. 2001;21(5):357–68. https://doi.org/10.1016/S0143-7496(01)00011-2.

[18] Dorn L, Liu W. The stress state and failure properties of adhesive-bonded plastic/metal joints. Int. J. Adhes. Adhes. 1993;13(1):21–31. https://doi.org/10.1016/0143-7496(93)90005-T.

[19] Aydin MD, Özel, e A. Temiz, The effect of adherend thickness on the failure of adhesively-bonded single-lap joints. J. Adhes. Sci. Technol. 19(8), 2005,:705–18. https://doi.org/10.1163/1568561054890499.

[20] Di Bella G, Galtieri G, Pollicino E, Borsellino C. Mechanical characterization of adhesive joints with dissimilar substrates for marine applications. Int. J. Adhes. Adhes. 2013;41:33–40. https://doi.org/10.1016/j.ijadhadh.2012.10.005.

[21] Gültekin K, Akpinar S, Özel A. The effect of moment and flexural rigidity of adherend on the strength of adhesively bonded single lap joints. J. Adhes. 2015;91 (8):637–50. https://doi.org/10.1080/00218464.2014.953674.

[22] Anes V, Pedro R, Henriques E, Freitas M, Reis L. Bonded joints of dissimilar adherends at very low temperatures – an adhesive selection approach. Theor. Appl. Fract. Mech. 2016;85:99–112. https://doi.org/10.1016/j.tafmec.2016.08.012.

[23] Ascione F, Lamberti M, Razaqpur AG, Spadea S. Strength and stiffness of adhesively bonded GFRP beam-column moment resisting connections. Compos. Struct. 2017;160:1248–57. https://doi.org/10.1016/j.compstruct.2016.11.021.

[24] El Zaroug M, Kadioglu F, Demiral M, Saad D. Experimental and numerical investigation into strength of bolted, bonded and hybrid single lap joints: effects of adherend material type and thickness. Int. J. Adhes. Adhes. 2018;87 (October):130–41. https://doi.org/10.1016/j.ijadhadh.2018.10.006.

[25] Razaqpur AG, Ascione F, Lamberti M, Spadea S, Malagic M. GFRP hollow column to built-up beam adhesive connection: mechanical behaviour under quasi-static, cyclic and fatigue loading. Compos. Struct. 2019;224:. https://doi.org/10.1016/j.compstruct.2019.111069111069.

[26] Kafkalidis MS, Thouless MD, Yang QD, Ward SM. Deformation and fracture of adhesive layers constrained by plastically-deforming adherends. J. Adhes. Sci. Technol. 2000;14(13):1593–607. https://doi.org/10.1163/156856100742401.

[27] Blackman BRK, Kinloch AJ, Paraschi M. The effect of the substrate material on the value of the adhesive fracture energy, Gc: further considerations. J. Mater. Sci. Lett. 2001;20(3):265–7. https://doi.org/10.1023/A:1006705808948.

[28] Blackman BR, Kinloch AJ, Paraschi M, Teo WS. Measuring the mode I adhesive fracture energy, G IC, of structural adhesive joints: the results of an international round-robin. Int. J. Adhes. Adhes. 2003;23(4):293–305. https://doi.org/10.1016/S0143-7496(03)00047-2.

[29] Pardoen T, Ferracin T, Landis CM, Delannay F. Constraint effects in adhesive joint fracture. J. Mech. Phys. Solids 2005;53(9):1951–83. https://doi.org/10.1016/j.jmps.2005.04.009.

[30] Kawashita LF, Kinloch AJ, Moore DR, Williams JG. The influence of bond line thickness and peel arm thickness on adhesive fracture toughness of rubber toughened epoxy-aluminium alloy laminates. Int. J. Adhes. Adhes. 2008;28 (4–5):199–210. https://doi.org/10.1016/j.ijadhadh.2007.05.005.

[31] Martiny P, Lani F, Kinloch AJ, Pardoen T. A multiscale parametric study of mode i fracture in metal-to-metal low-toughness adhesive joints. Int. J. Fract. 2012;173 (2):105–33. https://doi.org/10.1007/s10704-011-9667-x.

[32] ISO 527:2012, Plastics – Determination of tensile properties (2012)..

[33] W. Wang, R. Lopes Fernandes, S. Teixeira De Freitas, D. Zarouchas, R. Benedictus, How pure mode I can be obtained in bi-material bonded DCB joints: a longitudinal strain-based criterion, Compos. B Eng. 153. doi:10.1016/j.compositesb.2018.07.033..

[34] A. K. Kaw, Mechanics of Composite Materials, second ed., CRC Press, 2006. doi:10.1063/1.1988984. http://aip.scitation.org/doi/10.1063/1.1988984.

[35] Li G, Wang X, Li A, Wang W, Zheng L. Fabrication and adhesive properties of thin organosilane films coated on low carbon steel substrates. Surf. Coat. Technol. 2007;201:9571–8. https://doi.org/10.1016/j.surfcoat.2007.04.032.

[36] ASTM D 5528/ D 5528-13, Standard Test Method for Mode I Interlaminar Fracture Toughness of Unidirectional Fiber-Reinforced Polymer Matrix Composites, 2013. doi:10.1520/D5528-13.2. http://scholar.google.com/scholar?hl = en&btnG = Search&q = intitle:Standard + Test + Method + for + Mode + I

+ Interlaminar + Fracture + Toughness + of + Unidirectional + Fiber-Reinforced + Polymer + Matrix + Composites#2.

[37] Penado FE. A closed form solution for the energy release rate of the double Cantilever beam specimen with an adhesive layer. J. Compos. Mater. 1993;27:383–407. https://doi.org/10.1177/002199839302700403. http://journals.sagepub.com/doi/10.1177/002199839302700403.

[38] Kanninen MF. An augmented double cantilever beam model for studying crack propagation and arrest. Int. J. Fract. 1973;9:83–92.

[39] Heide-Jorgensen S, Budzik MK. Crack growth along heterogeneous interface during the DCB experiment. Int. J. Solids Struct. 2017;120:1339–51. https://doi.org/10.1016/j.ijsolstr.2017.05.013.

[40] Lefebvre DR, Dillard DA, Brinson HF. The development of a modified double-cantilever-beam specimen for measuring the fracture energy of rubber to metal bonds. Exp. Mech. 1988;28(1):38–44. https://doi.org/10.1007/BF02328994.

[41] Ouezdou MB, Chudnovsky A, Moet A. Re-evaluation of adhesive fracture energy. J. Adhes. 1988;25(3):169–83. https://doi.org/10.1080/00218468808071260.

[42] Budzik M, Jumel J, Shanahan ME. Adhesive compliance effect in mode I separation: profilometry approach. Int. J. Adhes. Adhes. 2011;31:135–45. https://doi.org/10.1016/j.ijadhadh.2010.11.012.

[43] Budzik M, Jumel J, Imielińska KI, Shanahan ME. Effect of adhesive compliance in the assessment of soft adhesives with the wedge test. J. Adhes. Sci. Technol. 2011;25:131–49. https://doi.org/10.1163/016942410X501133.

[44] M.W. Hyer, T.W. Knott, Analysis of the end-fitting-induced strains in axially loaded glass-epoxy cylinders, in: R.P. Reed, J.D. McColskey (Eds.), Composite Struts for SMES Plants (NISTIR 5024), 1994. arXiv:arXiv:1011.1669v3. doi:10.1016/S0167-8922(09)70001-X..

[45] Gonçalves JP, De Moura MF, De Castro PM. A three-dimensional finite element model for stress analysis of adhesive joints. Int. J. Adhes. Adhes. 2002;22(5):357–65. https://doi.org/10.1016/S0143-7496(02)00015-5.

[46] Qin G, Na J, Mu W, Tan W, Yang J, Ren J. Effect of continuous high temperature exposure on the adhesive strength of epoxy adhesive, CFRP and adhesively bonded CFRP-aluminum alloy joints. Compos. B Eng. 2018;154(5988):43–55. https://doi.org/10.1016/j.compositesb.2018.07.059.

[47] Chen B, Dillard DA. The effect of the T-stress on crack path selection in adhesively bonded joints. Int. J. Adhes. Adhes. 2001;21:357–68.

[48] Heide-Jørgensen S, Budzik MK. Effects of bondline discontinuity during growth of interface cracks including stability and kinetic considerations. J. Mech. Phys. Solids 2018;117:1–21. https://doi.org/10.1016/j.jmps.2018.04.002.